Demonstration of an ultralow profile cloak for scattering suppression of a finite-length rod in free space

Demonstration of an ultralow profile cloak for scattering suppression of a finite-length rod in free space

J C Soric[1]**, P Y Chen**[1]**, A Kerkhoff**[2]**, D Rainwater**[2]**, K Melin**[2,3] **and A Alù**[1,4]

[1] Department of Electrical and Computer Engineering, The University of Texas at Austin, Austin, TX 78712, USA
[2] Applied Research Laboratories, The University of Texas at Austin, Austin, TX 78758-4423, USA
[3] Department of Physics, The University of Texas at Austin, Austin, TX 78712, USA
E-mail: alu@mail.utexas.edu

Abstract. We present the first experimental realization and verification of a three-dimensional stand-alone *mantle cloak* designed to suppress the total scattering of a finite-length dielectric rod of moderate cross-section. Mantle cloaking has been proposed to realize ultralow-profile conformal covers that may achieve substantial camouflage, transparency and high-performance non-invasive near-field sensing. Here, we realize and verify a mantle cloak for radio-waves. We report an extensive campaign of far- and near-field free-space measurements demonstrating that conformal cloaks can indeed produce strong scattering suppression in all directions and over a relatively broad bandwidth of operation.

[4] Author to whom any correspondence should be addressed.

IOP Institute of Physics   **ⲫ** DEUTSCHE PHYSIKALISCHE GESELLSCHAFT

Contents

1. Introduction

Over the last decade there have been exciting advances in the area of electromagnetic and acoustic cloaking. A variety of theoretical approaches have been proposed and demonstrated through the application of metamaterials, aimed at reducing the scattering of various objects, ranging in size and material composition, and spanning low-frequencies [1–4], microwave [5–14] and near-optical regimes [15–20] (for an overview of the most popular cloaking methods, see the surveys in [21–23]). Cloaking is arguably one of the most fascinating topics in modern physics, made possible through the unique characteristics of metamaterials. These artificial materials allow new avenues to redirect wavefronts around an object, as in transformation [13, 24–27] and waveguide-based cloaks [28–30], or to suppress the scattering at all angles [6, 11, 31–32]. In recent works, we have shown that an alternative approach to invisibility, which we have named *mantle cloaking*, may be achieved using ultrathin *metascreens* rather than bulk metamaterials. These conformal patterned surfaces may possess similar exotic scattering properties as metamaterial covers, but may be easier and more practical to realize and may offer an improved bandwidth [33–37].

In the general sense, the experimental validation of the *cloaking* concept has until recently been limited to two-dimensional (2D) configurations in waveguides, due to the difficulties in realizing three-dimensional (3D) robust metamaterial covers with the required material parameters. In particular, the realization of transformation-based cloaks typically requires metamaterials with strong inhomogeneities and anisotropy, and with inherently resonant features, which may make them very sensitive to manufacturing imperfections, Ohmic losses, wave polarization and incidence angle. Therefore, while the metamaterial approaches have been visionary and exciting from the theoretical point of view, their realizations have so far been far from ideal, often limited to specific excitation angles and arguably of limited practical interest. 2D configurations in closed environments also inherently parry the major difficulties encountered with finite-length objects, namely oblique angles of incidence and end effects. Recently, a few exciting 3D experiments were reported in the microwave range using different techniques, such as the *plasmonic* [11–12] and the *metal-plate* [14] approaches, which appear to be inherently more robust than those based on transformation optics. In [11], extensive near-field and far-field measurements were presented to demonstrate a reduction in the total

scattering cross-section (SCS) of a finite-length dielectric rod using a plasmonic metamaterial cover. In [14] the scattering reduction of a finite-length metal-plate cloak was measured using bistatic far-field and forward scattering measurements in the microwave regime in order to estimate the scattering reduction at all viewing angles. It is not necessarily straightforward to apply the optical theorem to estimate the total SCS, as it requires very careful measurement conditions [38]. Another way to demonstrate reduction of the total SCS of an object is to measure its far-field bistatic cross-sections at various angles [11, 14], or map the fields in the near-field of the object [11].

Here we present the first experimental realization of *mantle cloaking* applied to a 3D finite-length cylinder. We achieve scattering cancellation with ultrathin conductive metasurfaces composed of subwavelength periodic elements. The patterned surface is tailored to realize an equivalent surface reactance that can scatter anti-phase fields to drastically suppress the scattering produced by a given stand-alone 3D object. Scattering cancellation is shown through measurements in the very near-field of the object, showing the restoration of the incident wavefront and realizing a moderately broadband cloaking phenomenon. One significant advantage of mantle cloaking is that the conformal patterned screen, or metasurface, can be easily implemented with printed technology, without requiring extreme values of bulk permittivity/permeability and/or anisotropies and inhomogeneities, as with other common metamaterial solutions to cloaking [5, 27]. The inherent conformability and low-profile of these surfaces may also allow the realistic possibility of cloaking arbitrarily shaped objects, extending the results in [39]. Recent works have also shown that the mantle cloaking method can be used to reduce antenna blockage and mutual coupling between co-sited antennas [34], opening novel practical avenues for the applications of cloaking. Additionally, exciting theoretical results have shown that mantle cloaking can be successfully extended to THz frequencies by leveraging the tunable conductivity of graphene monolayers of atomic thickness [23, 37].

The goal of this work is to experimentally verify the mantle cloaking approach envisioned in [33]. We demonstrate that this cloaking method is robust to practical limitations such as loss and design imperfections, and is effective for a large range of viewing angles. Our mantle cloak design is shown to significantly suppress the strongest scattering component at normal and near-normal incidence by over an order of magnitude and over a moderate bandwidth. For our experiment, as discussed in the following, we choose a dielectric rod of finite length and moderate cross-section, which poses some interesting challenges: (i) the field penetration inside the dielectric material can excite internal standing and surface waves along the dielectric rod, which manifest themselves as resonances at oblique incidence; (ii) the excitation of more than one significant scattering term may complicate the overall scattering signature of the object. Our experimental results open interesting venues by showing the practical applicability of mantle cloaking in a realistic configuration.

2. Mantle cloaking: theoretical background, design and simulations

2.1. Determination of the metasurface reactance at normal incidence for an infinite cylinder

Our goal is to achieve significant reduction of the *total* SCS of a 3D cylindrical object when covered by a properly designed passive metasurface, independent of the incidence angle of excitation. This goal is drastically different from low-observability or stealth techniques based on minimizing target backscatter, since they usually are not aimed at efficiently suppressing

the *total* scattering of the object, and especially its shadow[5]. The total SCS of a finite cylinder includes contributions from all relevant transverse-magnetic (TM) and transverse-electric (TE) scattered waves, scattering in all directions. Here, TM or TE polarized wavefronts define whether the magnetic or electric field lies in the plane orthogonal to the cylinder axis, respectively. The total scattering width (SW) is an analytically more tractable expression for the scattering from a 2D (infinite) cylinder, which approximates well the total SCS for large length-to-diameter aspect ratios. The total SW is generally defined as [38]

$$\sigma_{2D} = \frac{4}{k_0} \sum_{n=-\infty}^{\infty} \left(\left| c_n^{TM} \right|^2 + \left| c_n^{TE} \right|^2 \right), \tag{1}$$

where k_0 is the wavenumber of the background medium. The Mie scattering coefficients c_n^{TM} and c_n^{TE} represent the multipolar contributions to the total SW. For dielectric cylinders of moderate cross-section illuminated by TM or TE polarized wavefronts, c_0^{TM} and c_1^{TE} dominate the total SW, respectively. At normal incidence, these scattering coefficients are uncoupled; however, as the angle of incidence changes from normal incidence to smaller angles, TM–TE cross coupling becomes more relevant, which may increase the scattering and the overall visibility of cylindrical targets [32, 40–41]. At oblique incidence we are also prone to excite scattering resonances caused by the field penetration inside the dielectric, which can excite standing waves along the cylinder length [32, 40, 41]. Since the scattering from cylinders with moderate cross-section is in general larger at normal incidence than at oblique angles, we focus our design on the case of normal incidence, without considering the more complex effects arising for oblique excitation. We then analyze the performance and robustness of our design when the incidence angle changes.

Consider the geometry of figures 1(a) and (b), formed by a magnetodielectric 2D cylinder with constitutive parameters (μ, ε) illuminated in free space by a monochromatic TM plane wave under the $e^{-i\omega t}$ time convention. An ultrathin conformal cylindrical metasurface of radius a_c covers the dielectric rod of radius a, such that $a_c/a \simeq 1$. Provided that the granularity of the mantle cover is much smaller than the wavelength of operation, we may model the metasurface using an average surface current density **J**, associated with the discontinuity of the magnetic field across the thin cover. The surface impedance may then be related to this current density by Ohm's law: $\mathbf{E}_{tan} = \bar{\bar{\mathbf{Z}}}_\mathbf{s} \cdot \mathbf{J}$, where $\bar{\bar{\mathbf{Z}}}_\mathbf{s}$ is the surface impedance tensor and $\mathbf{E}_{tan}$ is the tangential component of the electric field, which is continuous across the metascreen cover. We assume in this section that the metascreen is lossless and, therefore, we may represent the equivalent surface impedance cover as purely reactive quantity $Z_s = -iX_s$.

For the geometry at hand, the incident and scattered fields are naturally represented by the Mie expansion in cylindrical harmonics [42]

$$\mathbf{E}_{tan} = \begin{cases} \hat{\mathbf{z}} E_0 \sum_{n=-\infty}^{\infty} i^n \left[a_n^{TM} J_n(k\rho) \right] e^{-in\varphi}, & \rho < a, \\ \hat{\mathbf{z}} E_0 \sum_{n=-\infty}^{\infty} i^n \left[b_n^{TM} J_n(k_c\rho) + d_n^{TM} Y_n(k_c\rho) \right] e^{-in\varphi}, & a < \rho < a_c, \\ \hat{\mathbf{z}} E_0 \sum_{n=-\infty}^{\infty} i^n \left[J_n(k_0\rho) + c_n^{TM} H_n^{(1)}(k_0\rho) \right] e^{-in\varphi}, & \rho > a_c. \end{cases} \tag{2}$$

[5] This implies that the object is less detectable only over a restricted range of observation angles. Typical in many scattering phenomena, the target backscatter is much reduced by sacrificing the forward scattering, or *shadow*, which may become quite large due to absorption.
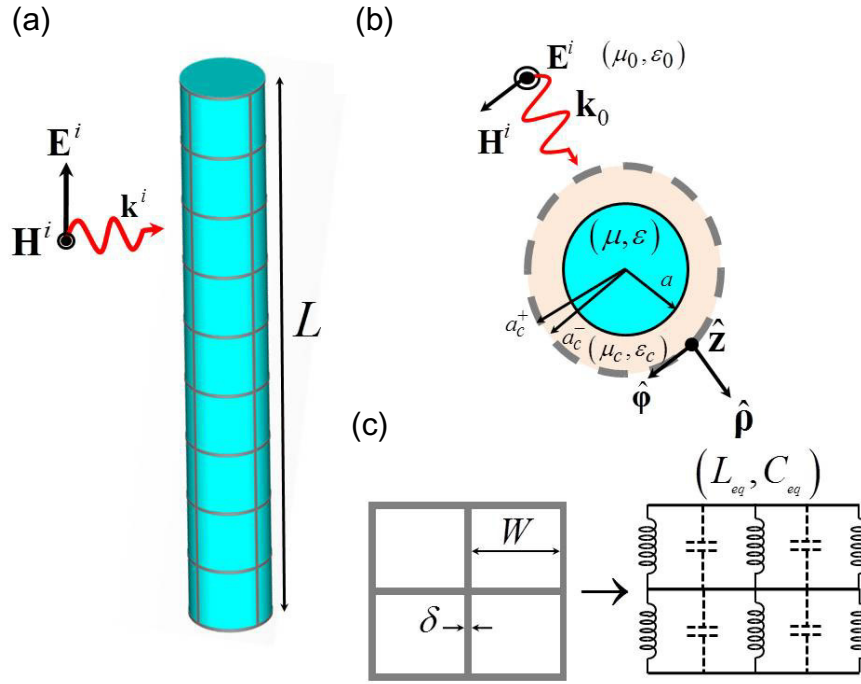
Figure 1. Magnetodielectric cylinder covered by a mantle metascreen and excited by a TM-polarized plane wave at normal incidence (a). Cross-section of the cylinder and of the conformal metascreen (b). Inductive surface reactance realized by a *fishnet* metascreen composed of subwavelength frequency-selective surface elements and its lumped equivalent circuit (c).

The corresponding incident and scattered magnetic fields may be found using the Maxwell–Faraday equation $\mathbf{H} = 1/\mathrm{i}\omega\mu\nabla \times \mathbf{E}$. In (2), $J_n(\cdot)$ and $H_n^{(1)}(\cdot)$ are the Bessel and Hankel functions of the first kind and order n representing standing and traveling cylindrical waves in each region, respectively [43]. For cylinders of moderate cross-section, the largest scattering contribution in figure 1(a) is due to TM polarization at normal incidence, for which the total electric field is purely along the cylinder axis and the impedance tensor $\bar{\bar{\mathbf{Z}}}_s$ may be expressed as a scalar. Continuity of the total tangential electric and magnetic fields on the single-layered metasurface interface in figure 1(b) yields [33]

$$\mathbf{E}_{\tan}|_{r=a_c^\pm} = Z_s \left(\mathbf{H}_{\tan}|_{r=a_c^+} - \mathbf{H}_{\tan}|_{r=a_c^-} \right). \tag{3}$$

Thus, the total field relations for each of the regions in figure 1(b) allows to write the expression of the Mie scattering coefficients succinctly as [31]

$$c_n^{\mathrm{TM}} = -\frac{U_n^{\mathrm{TM}}}{U_n^{\mathrm{TM}} + \mathrm{i}V_n^{\mathrm{TM}}}, \tag{4}$$

where

$$
U_n^{\text{TM}} = \begin{vmatrix} J_n(ka) & J_n(k_c a) & Y_n(k_c a) & 0 \\ \dfrac{J_n'(ka)}{\eta} & \dfrac{J_n'(k_c a)}{\eta_c} & \dfrac{Y_n'(k_c a)}{\eta_c} & 0 \\ 0 & J_n(k_c a_c) & Y_n(k_c a_c) & J_n(k_0 a_c) \\ 0 & \dfrac{Z_s}{\eta_c} J_n'(k_c a_c) - iJ_n(k_c a_c) & \dfrac{Z_s}{\eta_c} Y_n'(k_c a_c) - iY_n(k_c a_c) & \dfrac{Z_s}{\eta_0} J_n'(k_0 a_c) \end{vmatrix},
$$

$$
V_n^{\text{TM}} = \begin{vmatrix} J_n(ka) & J_n(k_c a) & Y_n(k_c a) & 0 \\ \dfrac{J_n'(ka)}{\eta} & \dfrac{J_n'(k_c a)}{\eta_c} & \dfrac{Y_n'(k_c a)}{\eta_c} & 0 \\ 0 & J_n(k_c a_c) & Y_n(k_c a_c) & Y_n(k_0 a_c) \\ 0 & \dfrac{Z_s}{\eta_c} J_n'(k_c a_c) - iJ_n(k_c a_c) & \dfrac{Z_s}{\eta_c} Y_n'(k_c a_c) - iY_n(k_c a_c) & \dfrac{Z_s}{\eta_0} Y_n'(k_0 a_c) \end{vmatrix}.
$$

(5)

In the determinants of (5), k_l and η_l are the wave numbers and impedances in each region l and $Y_n(\cdot)$ is Neumann function of order n. Derivatives in (5) are with respect to the arguments of $J_n(\cdot)$ and $Y_n(\cdot)$. By electromagnetic duality, similar expressions may be derived for TE-polarized excitation at normal incidence.

The Mie scattering coefficients c_n^{TM}, written as the ratio of the determinants U_n^{TM} and V_n^{TM}, quantify the conditions for scattering suppression, viz., $U_n^{\text{TM}} = 0 \Leftrightarrow |c_n^{\text{TM}}| = 0$, or resonance, $V_n^{\text{TM}} = 0 \Leftrightarrow |c_n^{\text{TM}}| = 1$ [31]. Therefore, by properly designing a surface reactance to meet the condition $U_n^{\text{TM}} = 0$, we may nullify any scattering contribution of order n at the frequency of interest. In general, the surface reactance required to cancel a particular scattering order, either TM or TE, will be different. Moreover, by nullifying a particular scattering order, we may risk to excite other scattering terms, since we may lie close to the condition $V_n = 0$ for other higher-order modes. Therefore, it is important to conduct a careful design of the cover to maximize bandwidth and overall scattering reduction [43].

Here we apply the concepts presented in [33, 35, 36] to create a patterned metasurface that may strongly reduce the total SCS of a finite-length dielectric cylinder with constitutive parameters $(3\varepsilon_0, \mu_0)$, as shown in figure 1. The length of the dielectric rod is $L = 18\,\text{cm} \approx 2.2\lambda_0$ and the 2D cross-section (figure 1(b)) is $2a = 24.9\,\text{mm} \simeq 0.31\lambda_0$, where the design frequency was chosen to be $f_0 = c/\lambda_0 = 3.73\,\text{GHz}$ and λ_0 is the free space wavelength. We have chosen a conformal design $(a_c/a \simeq 1)$ because of its ultralow profile and bandwidth performance [33, 35]. Figure 2 shows the required surface reactance as a function of frequency to cancel the dominant scattering term c_0^{TM}, calculated using equation (4). At the central frequency f_0 an inductive reactance $X_s = 195\,\Omega$ is needed.

Figure 3 shows the dispersion of the first four scattering coefficients for the bare (a), (c) and covered (b), (d) dielectric cylinders previously described, as calculated based on the above theory, assuming an ideal, homogeneous and infinitesimally thin surface impedance cover with the required reactance. As seen in the bare case, c_0^{TM} is by far the largest contribution due to an incident TM-polarized wavefront. However, there are also noticeable scattering contributions from TE harmonics (c). Our mantle cover is targeted to suppress the dominant scattering order, and indeed complete cancellation is observed at the design frequency (b). Interestingly, also the c_1^{TM} contribution is reduced at the design frequency f_0 and above. TE coefficients are also somewhat reduced by the cover (d) around the design frequency, but the cloak induces
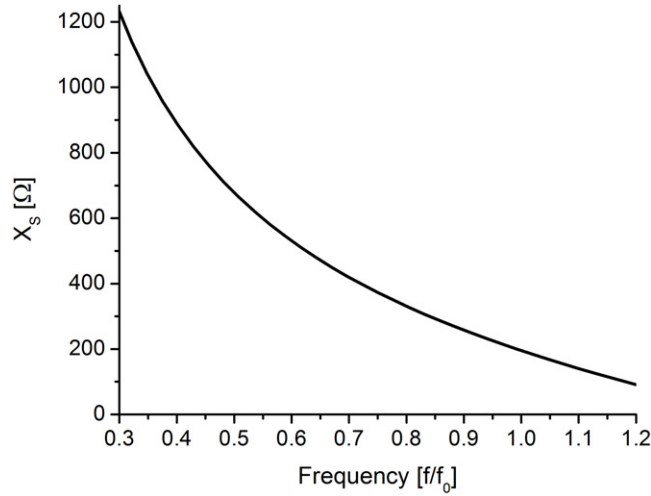
Figure 2. Required surface reactance to suppress the dominant scattering order for the geometry of figure 1 illuminated by a TM-polarized plane wave at normal incidence.
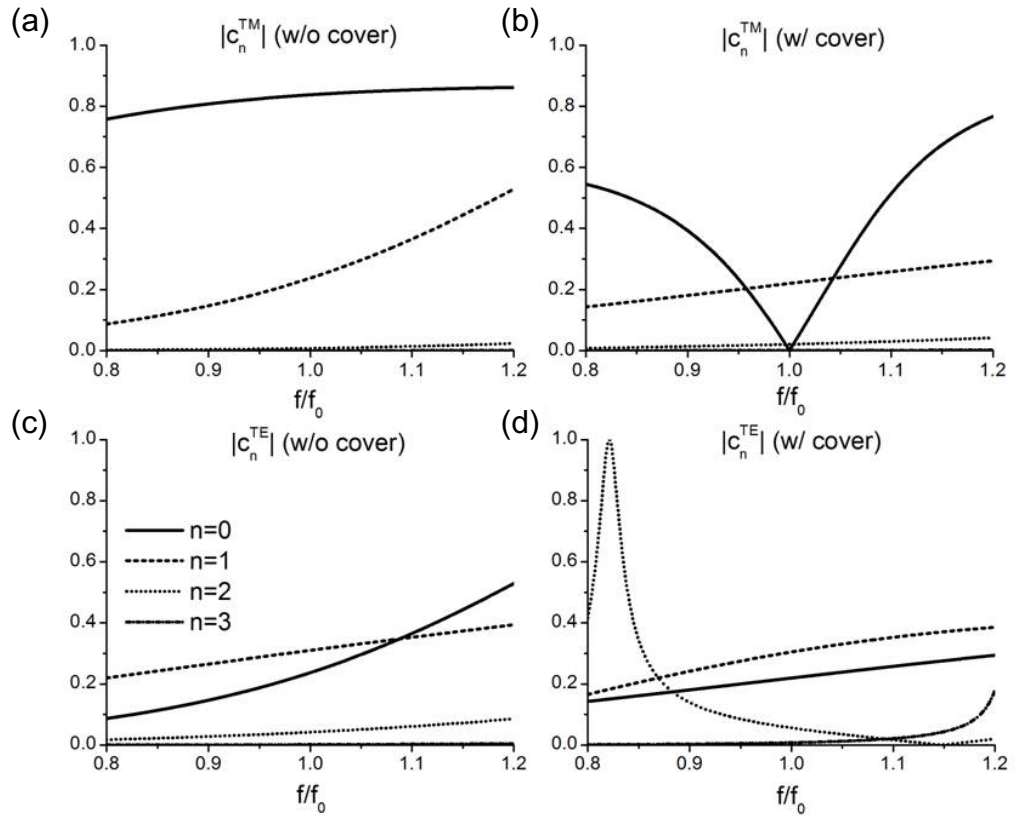

Figure 3. TM and electric scattering terms for the bare cylinder (a), (c) and the cylinder covered by an ideal $X_s = 195\,\Omega$ metascreen (b), (d).

a magnetic dipolar resonance ($V_1^{TE} = 0$) around $0.82 f_0$. While this effect will be reflected in scattering enhancement at lower frequencies, we expect strong total scattering reduction around the design frequency and for larger frequencies.
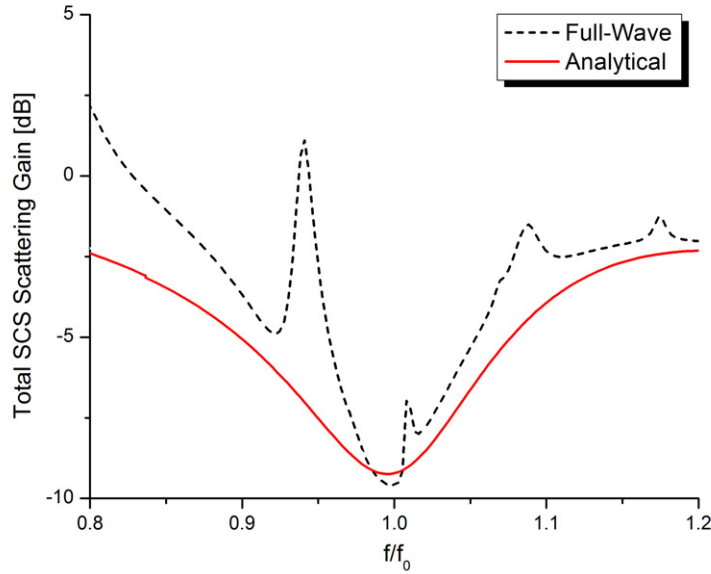
IOP Institute of Physics   Φ DEUTSCHE PHYSIKALISCHE GESELLSCHAFT

Figure 4. Analytical and full-wave simulations of the normalized total SCS.

2.2. Full-wave numerical analysis

We have used finite-integration simulations [44] to validate these analytical results for a realistic patterned surface tailored to synthesize the required shunt surface reactance in the case of a finite-length dielectric rod (figure 1). The optimized inductive metascreen consists of four longitudinal metallic traces running along the cylinder axis and ten circumferential traces (cf figure 1(c)), all with a line thickness $\delta = 1\,\text{mm} \simeq 0.01\lambda_0$. There are a total of 36 square apertures with $W \simeq 1.8\,\text{cm} \simeq 0.22\lambda_0$. We have verified that with good approximation we can neglect the metascreen losses here, due to the high conductivity of copper at microwave frequencies. The designed cover is tailored to realize the required surface reactance at the design frequency to suppress the dominant c_0^{TM} scattering term, as discussed in the previous section. The chosen fishnet configuration is well known to realize a compact, isotropic inductive response with a reduced parasitic capacitance between the conducting traces [45]. Our results in [36] have shown that analytical expressions to synthesize the required reactance in planar configurations may be safely used to design and tailor conformal metasurface designs with good accuracy, without the need of extensive optimization procedures.

Figure 4 compares analytical and simulated total SCS (integrated over all visible angles) for TM-polarized excitation at normal incidence. In the figure we simply show the *scattering gain*, defined as the scattering of the covered target normalized by that of the uncovered target at the same frequency, which allows an easy determination of the amount of overall scattering suppression. We can clearly see that strong scattering suppression is achieved over a moderately broad bandwidth, with largest scattering reduction around 9.6 dB at the design frequency. This is quite remarkable given the electrical cross-section of the target ($k_0 a \approx 1$) and its length, and the fact that this is obtained with a single conformal fishnet structure. The small disagreement between analytical and full-wave results, in particular the additional features visible in the full-wave spectrum, are due to the granularity of the realized metasurface. These non-idealities can be alleviated by using fewer circumferential traces; in the limit of
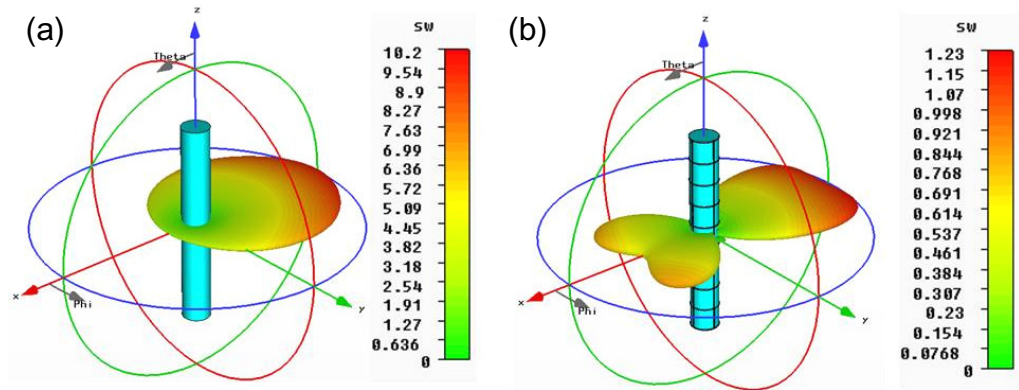
Figure 5. 3D far-field total scattering profiles for the uncloaked (a) and cloaked cases (b) at 3.73 GHz.
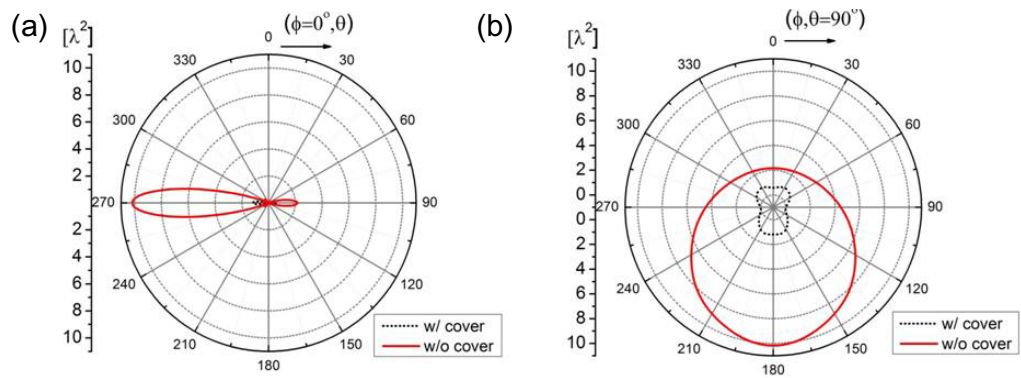

Figure 6. Principal plane elevation (a), and azimuthal (c) scattering profiles at 3.73 GHz.

thin cylindrical targets no circumferential strips are needed, since the scattering mechanism is dominated by the monopolar term, which for symmetry can be cancelled with longitudinal strips only. It is important to point out that it is difficult to simultaneously cancel several scattering multipoles at the same frequency with a single surface, due to the limited degrees of freedom. However, it may be possible to tailor the circumferential strips to cancel other relevant $c_n^{\mathrm{TE,TM}}$ scattering terms and further decrease the total SCS. We have not performed this optimization in the present work.

To better visualize the SCS reduction, figure 5 shows the calculated 3D far-field scattering profiles of the cloaked and uncloaked objects at the design frequency (notice the difference in scale), while figure 6 shows the SCS profiles along the principle plane cuts $\phi = 0°$ plane (figure 5(a)) and $\theta = 90°$ (figure 5(b)). Strong scattering reduction is observed over both principal planes, as expected. The figures confirm that the dominant monopolar scattering term is nearly cancelled and only residual higher-order scattering terms are left, producing residual and more directive scattering. This simple fishnet design is able to reduce the total scattering by over 85% at the design frequency.
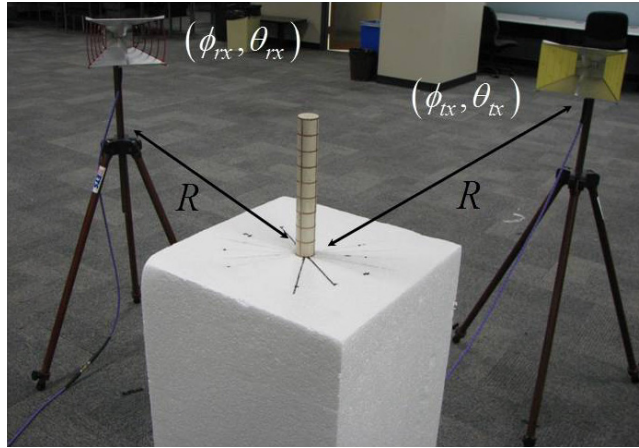
Figure 7. Far-field bistatic measurement setup. As shown in the schematic, the transmitter (ϕ_{tx}, θ_{tx}) and the receiver (ϕ_{rx}, θ_{rx}) are both at distance $R = 17.5\lambda_0$ from the region under test.

3. Measurement campaign

The optimized mantle cloak was fabricated using copper tape of thickness $66.0\,\mu\mathrm{m}$, trimmed and attached to a polycarbonate flexible film of thickness $100.0\,\mu\mathrm{m}$. Each of the conductive traces was cut to approximately 1 mm to realize the fishnet design in figure 1(c). To compare the measured results, all full-wave simulations considered losses with a non-ideal dielectric rod $\left(\delta = 0.002|_{f=3.7\mathrm{GHz}}\right)$ and copper tape $\left(\sigma = 5.8 \times 10^7\,\mathrm{S\,m^{-1}}\right)$.

3.1. Far-field measurements

Far-field bistatic measurements were performed to extract the radar cross-section (RCS) of the uncloaked and cloaked objects, and the extracted RCS was compared to full-wave simulations. Equal distances between the transmitter (ϕ_{tx}, θ_{tx}) and receiver (ϕ_{rx}, θ_{rx}) to the target were maintained at $R = 17.5\lambda_0$ while scanning over principal elevation and azimuthal planes as in figure 5, using calibrated ETS-Lindgren 3115 ultra-wideband horn antennas, shown in figure 7. Transmission data were acquired through an Agilent E5071C vector network analyzer, which measured the raw complex scattering response between the two antennas as the scattering parameter $\mathbf{S_{21}}$. In figure 7, as an example, we show the azimuthal bistatic measurement when the transmitter is located at $(\phi_{tx} = 0°, \theta_{tx} = 90°)$ and the receiving antenna is moved in the azimuth plane $(\phi_{rx} = 90°, \theta_{rx} = 90°)$.

Repositioning the antennas around the target at a constant target distance achieved the desired monostatic or bistatic measurements. Our non-anechoic laboratory environment necessitated vector background subtraction and software-based time gating steps in post-processing to remove background clutter. Background subtraction requires two measurements: one with the target in place, yielding $\mathbf{S_{21,T}}$, and another with only the target removed, yielding $\mathbf{S_{21,B}}$. The quantity $\mathbf{S_{21,S}} = \mathbf{S_{21,T}} - \mathbf{S_{21,B}}$ closely corresponds to the response of the target with most environmental effects removed. Software-based time gating further reduces clutter. This
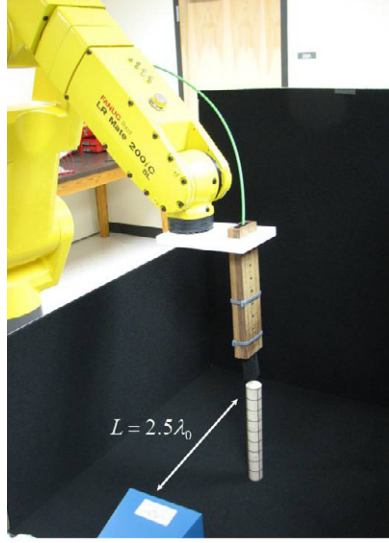
Figure 8. Picture of the near-field mapping system. A microwave horn excites each test scenario and a near-field probe samples the temporal and spatial TM-polarized electric field.

processing step is expressed as

$$\mathbf{S}'_{21,\mathbf{S}} = \text{fft}[\mathbf{W} \cdot \text{ifft}(\mathbf{S}_{21,\mathbf{s}})], \tag{6}$$

where $\text{fft}(\cdot)$ and $\text{ifft}(\cdot)$ are the fast Fourier transform and its inverse, and $\mathbf{W}$ is a rectangular window function used to gate out returns due to the background clutter.

Post-processed S-parameter measurements were converted to RCS values using the radar range equation [46]

$$\left|\mathbf{S}'_{21,\mathbf{s}}\right|^2 = \frac{P_r}{P_t} = \frac{G_t G_r \lambda_0^2 \sigma}{(4\pi)^3 \, R_t^2 R_r^2}, \tag{7}$$

where P_r and (P_t) are the received and (transmitted) power, G_r and (G_t) are the receive and (transmit) gain, and R_r and (R_t) are the distances from the cloaked dielectric cylinder to the receive and (transmit) antennas. Substituting measured and known values (including antenna gain calibration values), one can solve for the RCS (σ).

To achieve high temporal resolution in the time gating step, measurements were performed over a wide frequency band of 1–5 GHz. The difference in $\mathbf{S}'_{21,\mathbf{S}}$ between the two measurements yields the metric scattering gain, which quantifies the scattering reduction by normalizing the cloaked RCS to the uncloaked RCS. To demonstrate and validate the time gating and background procedure, figure 9 overlays the raw RCS data with the post-processed time-gated data for a sample measurement in the forward direction. Panel (a) shows the raw measurements of the object along with the covered object, and (b) shows the scattering gain, both with and without time gating. It is clear that the forward scattering is significantly reduced, even beyond our measurement bandwidth, and the scattering gain shows more than 10 dB reduction over a moderate bandwidth. The optical theorem ensures that the total scattering is similarly reduced, in agreement with our full-wave simulations of figure 4. Additionally, it is seen that the time-gating matches the raw response extremely well. We note that some error is inevitably
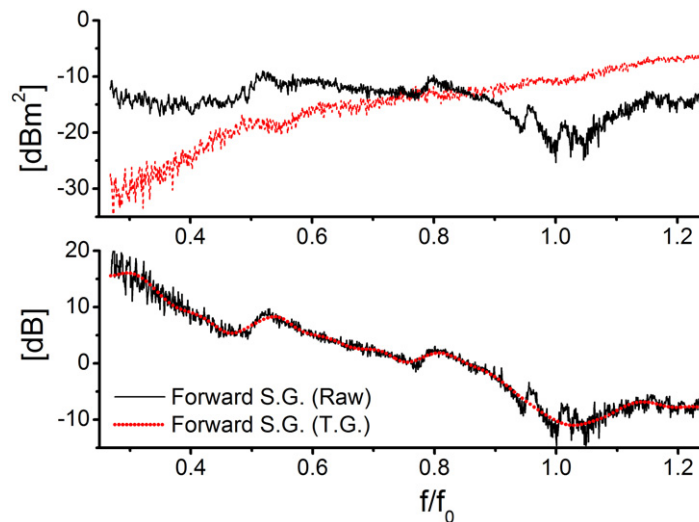
Figure 9. (a) Raw RCS data measured in the forward direction of the uncovered (dashed) and covered (solid) cylinder; (b) comparison of the computed scattering gain (S.G.) in the same direction obtained from raw RCS data and time-gated (T.G.) data.

introduced by filtering out the unintended returns in the time domain. The most significant errors are introduced near the edges of the data acquisition bandwidth, but these regions are far outside the designed bandwidth.

Figure 10 shows the measured and simulated scattering gains in the azimuthal plane, where the transmit antenna was held constant at ($\phi_{tx} = 0°$, $\theta_{tx} = 90°$), while the receive antenna was moved throughout the range ($30° \leqslant \phi_{rx} \leqslant 180°$, $\theta_{rx,tx} = 90°$). We can see that the strongest scattering contribution at normal incidence is significantly reduced by applying the cloak around the design frequency. The frequency of maximum scattering reduction is seen to move up in frequency from boresight to the forward scattering direction, consistent with our simulations. As will be shown in the near-field maps in the next section, this varying azimuthal scattering dip leads to an increased bandwidth of overall total SCS reduction, and is due to the complex interaction between the anisotropic effective surface impedance realized by our cover and the higher-order scattering terms, as shown in figure 3. Remarkably, we may observe a 13 dB reduction in forward scattering, which is typically the most difficult to suppress in cloaking experiments (figure 9).

The minor differences between measurements and simulations are attributed to the slight variation in the metascreen prototype. The realized traces were measured to have up to 5% error in width, corresponding to a maximum of 5% error in operating frequency, due to the nearly linear surface impedance dispersion around f_0 (see figure 2). It is also important to notice the difference in the strength of scattering gain dips between simulated and measured results. These differences are attributed to two main reasons: first, as shown in figure 9, the post-processing in the time gating step makes somewhat smooth the measured data depending on the length of the rectangular window. In removing the background clutter, we also necessarily remove some of the details of the scattering from the realistic anisotropic surface impedance. For instance, the anisotropic effects of the metascreen are more apparent in the simulations and raw data
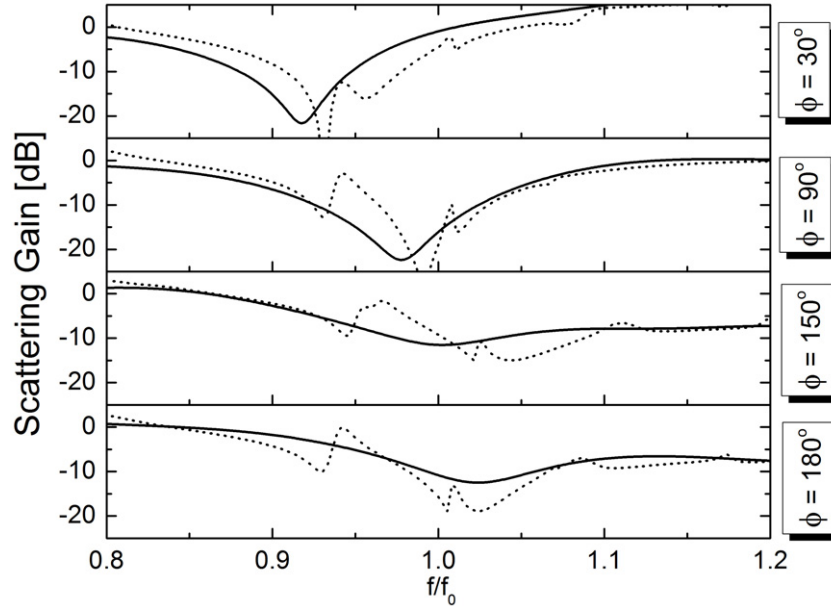
Figure 10. Bi-static scattering gain for normal incidence $30° \leqslant \phi \leqslant 180°$, $\theta_{\mathrm{rx,tx}} = 90°$ and various azimuthal receiver angles: measurements (solid) and simulations (dotted) are compared in each panel.

(see figure 9) than in the post-processed data in figure 10. To a lesser degree, while ideally small losses were considered in our simulations, differences due to manufacturing tolerances in the dielectric material, copper tape and polycarbonate sheet may have led to slightly more absorption in the cover and dielectric rod, thereby decreasing the sharpness of the cloaking dip in the realistic setup. Still, the agreement between simulations and measurements is good overall, and the trend of the cloaking dip as a function of angle is quite accurate.

Similarly, figure 11 shows a scan in the elevation plane for the case in which the transmitting antenna was held in the same location ($\phi_{\mathrm{tx}} = 0°$, $\theta_{\mathrm{tx}} = 90°$) while the receiving antenna was moved between ($\phi_{\mathrm{rx}} = 0°$, $-60° \leqslant \theta_{\mathrm{tx}} \leqslant 30°$) in steps of $30°$. The elevation measurements show more resonant features and relatively less agreement with the numerical simulations, but a consistent scattering reduction is observed around the frequency of interest, and the general trends are similar. As discussed above, time gating and realistic absorption may be responsible for some of the differences between the locations and depths of the resonances between the simulated and measured results in figure 11.

As derived in [36], the fishnet design is characterized by an impedance varying with angle of incidence as

$$X_{\mathrm{s}} = -\frac{f \eta_0 D}{c} \ln\left[\csc\left(\frac{\pi w}{2D} \right) \right] \left(1 - \frac{\cos^2 \theta_{\mathrm{s}}}{\varepsilon_{\mathrm{r}} + 1} \right), \tag{8}$$

where D is the period, w is the width of the traces, f is the frequency of interest, c is the speed of light, θ_{s} is the incidence angle measured from $\hat{z}$ (see figure 1(b)) and ε_{r} is the relative permittivity of the dielectric object. Therefore, as the elevation angle increases, the effective surface impedance is lowered. For instance, we predict from equation (8) a reduction of approximately $39\,\Omega$ between normal ($\theta = 90°$) and ($\theta = 30°$) incidence. As shown in figure 2, this lowering leads to an increase of the cloaking frequency, up to 8% at $\theta = 30°$, which explains
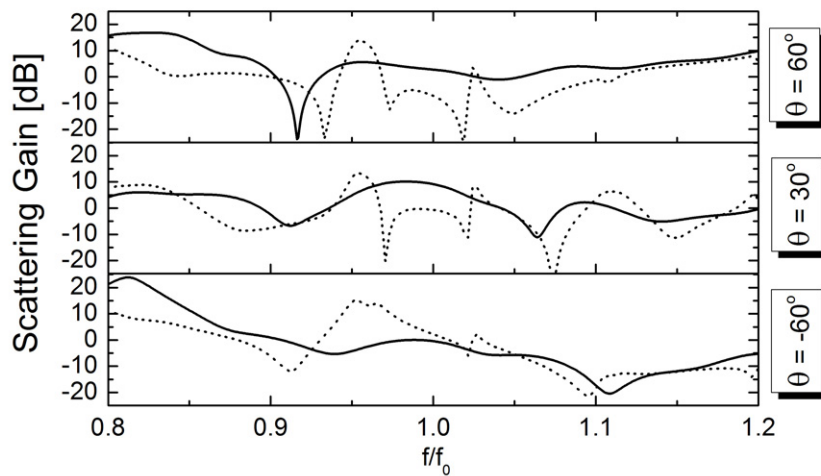
Figure 11. Bi-static scattering gain for $\phi_{tx,rx} = 0°$ and various elevation angles: measurements (solid) and simulations (dotted) are compared in each panel.

the trend in figure 11. The residual and more directive higher-order terms also add another layer of complexity to the measured spectra, especially for oblique incidence, consistent with the TE scattering term dispersion predicted in figure 3. Our design keeps suppressing the dominant term for larger incidence angles; however, the frequency of operation is varied.

It should be finally pointed out that, although at some angles the scattering gain is above 0 dB at the design frequency, in the elevation plane the overall scattering is significantly less than in the principal plane, especially for large incidence angles, consistent with figures 5 and 6. It is evident that suppressing the scattering at all angles with a single metasurface is not necessarily possible, but, by integrating over all the visible angles, as done in figure 4, significant total SCS suppression may be achieved. We predict that better results may be obtained by considering multiple stacked metasurfaces, or by tailoring a single surface to fit the required surface reactance curve over a broader frequency range, that may be able to suppress several scattering orders at the same frequency. It should be also stressed that figure 11 shows the scattering gain, i.e., the normalized scattering to the uncloaked scenario, and for oblique incidence the scattering may be significantly smaller than for normal incidence, weighing less on the total SCS of the object.

3.2. Near-field mapping

In addition to far-field measurements, we have conducted several near-field scans to visualize more strikingly the scattering reduction by the mantle cloak around the object. Our 3D near-field scanning system was programmed to map the temporal and spatial total electric field distribution around the device under test, similar to our setup in [11]. In this case, the illuminating microwave horn, polarized parallel to the cylinder's axis, was placed at $2.6\lambda_0$ from the target (cf figure 8). The scan area was $2.4\lambda_0 \times 2.4\lambda_0$ with a fine sampling resolution $\Delta x = \Delta y = 0.08\lambda_0$. Three different scenarios are presented in figure 12: (i) uncloaked, (ii) cloaked and (iii) free-space. In each case, the near-field probe was held at a constant height of approximately 80% of the cylinder height L (see figure 1(a)) in the azimuthal plane, except for the case when the sampling plane intersected the region of the object. The black squares in figure 12 are the regions where
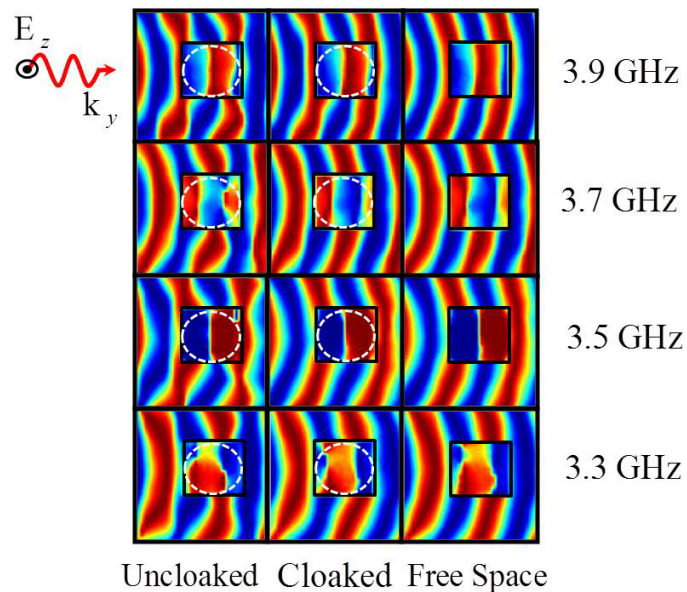
Uncloaked Cloaked Free Space

Figure 12. Snapshot in time of the normal electric field distribution for the azimuthal plane. A microwave horn illuminates each test scenario with a TM-polarized Gaussian wavefront at normal incidence.

the near-field probe was programmed to scan directly above the object (in a different plane) to avoid collision and the dashed white circle represents the location of the dielectric rod.

It is seen that the Gaussian wavefronts radiated by the horn are well restored by the cloak, and are nearly identical to the free-space case. Best cloaking performance is observed in the frequency band $3.3 - 3.9$ GHz, which demonstrates the moderately broad bandwidth of this cloaking technique. The experimental results show good agreement with our numerical modeling results in the previous section. In figure 12, the edges of the operation band are also shown (top and bottom rows), which, as expected, provide a somewhat weaker performance than in the design band 3.6–3.8 GHz. The third row shows the best scattering reduction performance at 3.7 GHz, consistent with the simulated total SCS results in figure 3. Here, the phase fronts around and on top of the cloaked object are nearly indistinguishable from the one measured in free-space, and it is impressive to notice the restored near-field field distribution, even just outside the thin cloaking layer, further illustrating the scattering cancellation induced by the metasurface. At 3.3 and 3.9 GHz, which are respectively the lower and upper bound of the cloaking operation, we can still find suppression of the near-field scattering, when compared to the uncloaked dielectric rod.

We have also tested the near-field distribution for oblique illumination. The results in the previous sections showed that the cloaking effect was maintained at oblique incidence, but the optimal cloaking dip was effectively *blue-shifted* with increasing incidence angles. This is confirmed and visually demonstrated in our measured near-field maps in figure 13, which considers the case of illumination at a $30°$ elevation angle. This is an extreme case, for which the target is nearly parallel to the azimuthal plane of measurement. Also in this case the field snapshots are taken in the azimuthal plane at a constant height, except for the positions for which the cloak or object (black outline) would hit the near-field probe. The white-dashed line
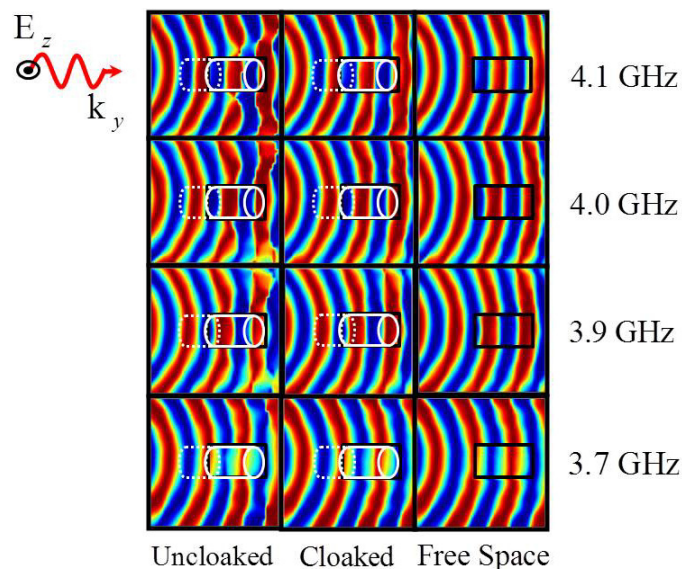
Figure 13. Snapshot in time of the electric near-field distribution for the azimuthal plane for 30° incidence.

in the figure corresponds to the points where the object under test is below the measurement plane and the probe plane did not need to be moved. The incident fields are shown to be only slightly disturbed by the presence of the covered dielectric rod for frequencies around the design frequency and higher. Here we should note that, due to the experimental setup, the end of the uncloaked and cloaked dielectric cylinders are fully exposed (not covered by the mantle cloak) to the incident field. However, the cross-sectional area at the end of the object is quite small, so it only adds a marginal amount to the total SCS. Overall, the cloaking effect due to the conformal metasurface shows strong suppression between 3.7 and 4.1 GHz for this excitation angle, consistent with our numerical results and far-field measurements.

4. Conclusions

We have reported here the first experimental verification of mantle cloaking for a 3D finite-length dielectric cylinder of moderate cross-section. We have shown good scattering suppression over a broad range of viewing angles and over a moderate frequency range using a simple ultrathin patterned metascreen tailored to suppress the dominant scattering order. Higher-order multipoles can contribute to the residual scattering and it is foreseen that the use of multiple mantle layers or an asymmetric tailoring of the cloak may be optimized to suppress more scattering orders, especially for larger objects. The observed scattering reduction was not limited to far-field observers, but it was also verified right around the cloaked object. As demonstrated in this work, cloaking in the very near-field by means of an equivalent surface reactance guarantees strong scattering suppression for arbitrary wavefronts, showing that the conformal metascreen cloak is resilient to complex and non-ideal phase patterns, as theoretically explored in [47]. Combined with the field penetration inside the cloak, these results pave the way to realizing not only 3D conformal camouflaging and invisibility, but also a practical scheme for non-invasive high-performance near-field sensors [48]. The ease of fabrication of our design is very

IOP Institute of Physics **Φ** DEUTSCHE PHYSIKALISCHE GESELLSCHAFT

appealing, especially at microwave frequencies, as opposed to other more complex cloaking strategies, and the realized prototype tested in this work also shows a strong invariance to manufacturing and measurement imperfections as well as realistic losses.

Acknowledgments

References

[1] Norris A N 2008 *Proc. R. Soc. Lond.* A 2008 **464** 2411
[2] Farhat M, Enoch S, Guenneau S and Movchan A B 2008 *Phys. Rev. Lett.* **101** 134501
[3] Guild M D, Haberman M R and Alù A 2011 *Wave Motion* **48** 468
[4] Popa B I, Zigoneanu L and Cummer S A 2011 *Phys. Rev. Lett.* **106** 253901
[5] Schurig D, Mock J J, Justice B J, Cummer S A, Pendry J B, Starr A F and Smith D R 2006 *Science* **314** 977–80
[6] Edwards B, Alù A, Silveirinha M and Engheta N 2009 *Phys. Rev. Lett.* **103** 153901
[7] Liu R, Ji C, Mock J J, Cui J Y and Smith D R 2009 *Science* **323** 366
[8] Alitalo P, Bongard F, Zurcher J F, Mosig J and Tretyakov S A 2009 *J. Appl. Phys.* **94** 014103
[9] Tretyakov S A, Alitalo P, Luukkonen O and Simovski C 2009 *Phys. Rev. Lett.* **103** 103905
[10] Bao D, Rajab K Z, Hao Y, Kallos E, Tang W, Argyropoulos C, Piao Y and Yang S 2011 *New J. Phys.* **13** 103023
[11] Rainwater D, Kerkhoff A, Melin K, Soric J C, Moreno G and Alù A 2012 *New J. Phys.* **14** 013054
[12] Xu S *et al* 2012 *Phys. Rev. Lett.* **109** 223903
[13] Landy N and Smith D R 2012 *Nature Mater.* **12** 25
[14] Alitalo P, Culhaoglu A E, Osipov A V, Thurner S, Kemptner E and Tretyakov S A 2012 *J. Appl. Phys.* **111** 034901
[15] Valentine J, Zhang S, Zentgraf T, Ulin-Avila E, Genov D A, Bartal G and Zhang X 2008 *Nature* **455** 376
[16] Gabrielli L H, Cardenas J, Poitras C B and Lipson M 2009 *Nature Photon.* **3** 461
[17] Ergin T M, Stenger N, Brenner P, Pendry J B and Wegener M 2010 *Science* **328** 337
[18] Zhang B, Luo Y, Liu X and Barbastathis G 2011 *Phys. Rev. Lett.* **106** 033901
[19] Chen X, Luo Y, Zhang J, Jiang K, Pendry J B and Zhang S 2011 *Nature Commun.* **2** 176
[20] Aliev A E, Garstein Y N and Baughman R Y 2011 *Nanotechnology* **22** 435704
[21] Alù A and Engheta N 2008 *J. Opt. A: Pure Appl. Opt.* **10** 093002
[22] Alitalo P and Tretyakov S A 2011 *Proc. IEEE* **99** 1646
[23] Chen P Y, Soric J and Alù A 2012 *Adv. Mater.* **24** OP281
[24] Pendry J B, Schurig D and Smith D R 2006 *Science* **312** 1780
[25] Leonhardt U 2006 *Science* **312** 1777
[26] Li Jensen and Pendry J B 2008 *Phys. Rev. Lett.* **101** 203901
[27] Landry N and Smith D R 2013 *Nature Mater.* **12** 25
[28] Alitalo P, Luukkonen O, Jylha L, Venermo L and Tretyakov S A 2008 *IEEE Trans. Antennas Propag.* **56** 416
[29] Tretyakov S A, Alitalo P, Luukkonen O and Simovski C 2009 *Phys. Rev. Lett.* **103** 103905
[30] Alitalo P, Culhaoglu A E, Osipov A V, Thurner S, Kemptner E and Tretyakov S A 2012 *IEEE Trans. Antennas Propag.* **60** 4963
[31] Alù A and Engheta N 2005 *Phys. Rev.* E **72** 016623
[32] Alù A, Kerkhoff A and Rainwater D 2010 *New J. Phys.* **12** 103028

IOP Institute of Physics **Φ** DEUTSCHE PHYSIKALISCHE GESELLSCHAFT

[33] Alù A 2009 *Phys. Rev.* B **80** 245115
[34] Monti A, Soric J, Alù A, Bilotti F, Toscano A and Vegni L 2012 *IEEE Antennas. Propag. Lett.* **11** 1414
[35] Chen P Y and Alù A 2011 *Phys. Rev.* B **84** 205110
[36] Padooru Y R, Yakovlev A B, Chen P Y and Alù A 2012 *J. Appl. Phys.* **112** 034907
[37] Chen P Y and Alù A 2011 *ACS Nano* **5** 5855
[38] Bohren C F and Huffman D R 1983 *Absorption and Scattering of Light by Small Particles* (New York: Wiley)
[39] Tricarico S, Bilotti F, Alù A and Vegni L 2010 *Phys. Rev.* E **81** 026602
[40] Seker S S and Schneider A 1988 *IEEE Trans. Antennas Propag.* **36** 303
[41] Yousif H A, Mattis R E and Kozminski K 1994 *Appl. Opt.* **33** 4013
[42] Balanis C A 1989 *Advanced Engineering Electromagnetics* (New York: Wiley)
[43] Abramowitz M and Stegun I A (ed) 1972 *Handbook of Mathematical Functions with Formulas, Graphs and Mathematical Tables* 9th edn (New York: Dover)
[44] CST Microwave Studio 2012 www.cst.com
[45] Munk B A 2000 *Frequency Selective Surfaces: Theory and Design* (New York: Wiley)
[46] Balanis C A 2005 *Antenna Theory: Analysis and Design* (New York: Wiley)
[47] Padooru Y R, Yakovlev A B, Chen P Y and Alù A 2012 *J. Appl. Phys.* **112** 104902
[48] Alù A and Engheta N 2009 *Phys. Rev. Lett.* **102** 233901